

SCIENTIFIC REPORTS



OPEN

Intrinsic beam emittance of laser-accelerated electrons measured by x-ray spectroscopic imaging

G. Golovin¹, S. Banerjee¹, C. Liu¹, S. Chen¹, J. Zhang¹, B. Zhao¹, P. Zhang¹, M. Veale², M. Wilson², P. Seller² & D. Umstadter¹

Received: 08 December 2015

Accepted: 30 March 2016

Published: 19 April 2016

The recent combination of ultra-intense lasers and laser-accelerated electron beams is enabling the development of a new generation of compact x-ray light sources, the coherence of which depends directly on electron beam emittance. Although the emittance of accelerated electron beams can be low, it can grow due to the effects of space charge during free-space propagation. Direct experimental measurement of this important property is complicated by micron-scale beam sizes, and the presence of intense fields at the location where space charge acts. Reported here is a novel, non-destructive, single-shot method that overcame this problem. It employed an intense laser probe pulse, and spectroscopic imaging of the inverse-Compton scattered x-rays, allowing measurement of an ultra-low value for the normalized transverse emittance, $0.15 (\pm 0.06) \pi \text{ mm mrad}$, as well as study of its subsequent growth upon exiting the accelerator. The technique and results are critical for designing multi-stage laser-wakefield accelerators, and generating high-brightness, spatially coherent x-rays.

Interest in laser-wakefield electron accelerators¹ (LWFA) has been principally motivated by their ultrahigh acceleration gradient, which is $1,000\times$ greater than that of conventional (RF-based) alternatives. Advances in LWFA technology have also recently led to the development of a new generation of x-ray sources, including ones based on inverse-Compton-scattering (ICS), betatron emission, or free-electron lasing². These accelerators and photon sources have the advantage of being small enough to fit in a university or hospital laboratory. Also, both types of beams, electron^{3,4} and x-ray^{5–7}, are demonstrated to be energetic, narrow in bandwidth, tunable and have micron source size. Additionally, their pulse duration are either demonstrated (in the case of electrons) or expected (in the case of x-rays) to be just a few femtoseconds in duration^{8,9}. These unique beam characteristics are creating new opportunities in basic and applied research^{2,10}, such as (1) time-resolved diffraction^{11,12} for studies of ultrafast dynamics¹³, (2) nanoscale critical-dimension small-angle scattering¹⁴ for advanced semiconductor metrology, (3) micron-scale-resolution radiography¹⁵ for non-destructive evaluation, and (4) phase-contrast imaging^{16,17} and low dose radiology¹⁸ for bio-medical imaging.

The bandwidth, spatial coherence and spectral brightness of accelerator-based x-ray beams all depend critically on transverse electron-beam emittance. The high-field gradients (GeV/cm) of laser-wakefield electron accelerators should in principle result in low emittance beams. However, as the beams freely propagate in the vacuum region after acceleration, space-charge effects will cause the emittance to rapidly increase. Direct measurement of intrinsic emittance (before space charge acts) has posed a substantial challenge for several reasons¹⁹.

First, LWFA electron beams differ significantly from those produced by conventional methods. They have an order of magnitude larger energy and angular spread, orders of magnitude smaller source size, significantly smaller transverse emittance, shorter pulse duration, and lower shot-to-shot reproducibility. Second, because of their higher charge density, and hence space charge effects, the electron beam emittance is predicted by numerical simulations^{20,21} and theoretical modeling²² to grow rapidly as the electron beam freely propagates in vacuum away from the accelerator exit. Third, the high-intensity laser light co-exists simultaneously in the same region where the space charge acts. For these reasons, prior emittance measurements of LWFA electron beams have been unable to account for this space charge growth.

For example, the pepper-pot technique^{20,23–25} was recently shown to overestimate the emittance of electron beams that have a source size smaller than $10 \mu\text{m}$ ¹⁹, as is the case with LWFA beams²⁶. Betatron emission has also

¹Department of Physics and Astronomy, University of Nebraska, Lincoln NE 68588, USA. ²Science and Technology Facilities Council, Rutherford Appleton Laboratory, Harwell Science & Innovation Campus, Didcot OX11 0QX, UK. Correspondence and requests for materials should be addressed to D.U. (email: donald.umstadter@unl.edu)

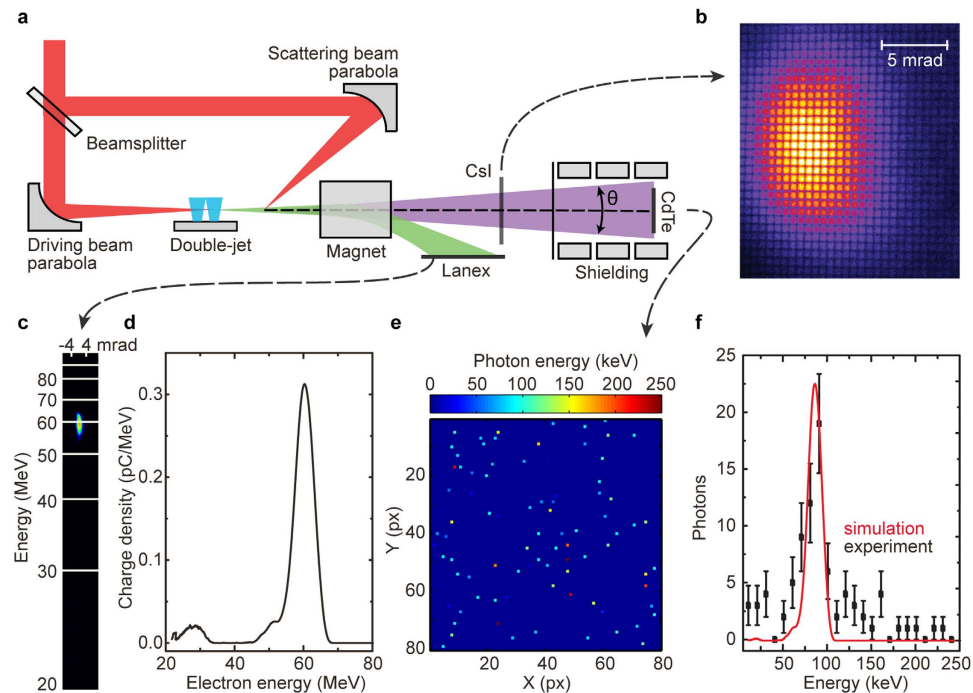


Figure 1. Layout of the experimental setup and a typical single-shot dataset. (a) Experimental setup. Spectral characteristics of an electron beam are measured using a magnetic spectrometer and a fluorescent LANEX screen. X-ray beam imaging is performed with high (0.4 mrad) angular resolution (as a function of polar angle θ) using the CdTe spectroscopic x-ray imaging detector. See Methods for additional information. (b) The x-ray profile measured with a CsI scintillator coupled to a 14-bit high-gain CCD. When the CdTe detector was operated, the CsI was removed from the path of the x-ray beam. (c) LANEX image of the dispersed electron beam. (d) Reconstructed electron beam spectrum based on the response function of the magnetic spectrometer. The beam has a charge of 2.4 ± 0.4 pC, central energy of 60 ± 1 MeV, and $10 \pm 1\%$ energy spread (FWHM). (e) Measured x-ray signal on the CdTe detector with charge sharing correction. Each dot represents a single photon event. (f) X-ray spectrum, measured with the CdTe detector (black, error bars represent standard deviations based on Poisson statistics), central energy is 85 ± 1 keV with $24 \pm 2\%$ energy spread (FWHM, averaged over 6-mrad cone) and simulated spectrum based on the electron beam spectrum (red). Figures (c–f) correspond to the same shot.

been used to estimate the emittance of laser-driven electron beams, but only inside, and averaged over, the plasma acceleration region^{27,28}. The reported emittance is likely different from the free-space value after the electron beam exits the plasma. Likewise, quadrupole scanning²⁹ is unable to measure intrinsic electron-beam emittance.

We report experimental results of a novel measurement technique that overcomes the aforementioned problems. We use spectroscopic imaging of ICS x-rays^{30–32} to extract electron beam signatures imprinted on the spatial and spectral characteristics of the scattered x-rays, and measure the electron beam energy, energy spread, angular divergence, and source size. These parameters were used to determine the intrinsic electron-beam transverse emittance immediately at the exit of the accelerator, and after 40 cm of propagation. The observed significant change of both the angular divergence and transverse emittance is found to be consistent with the predictions of theoretical models^{22,33}, as well as with our own numerical simulations.

Results

The experimental setup is shown in Fig. 1(a). A high-energy, ultrashort pulse from a Ti:Sapphire laser system is split in two using a beamsplitter, each part is then independently compressed. The first pulse is used to accelerate electron beams in the double-stage gas target via the process of laser-wakefield acceleration. The second pulse scatters from the electron beam at an angle of 170 deg. and generates x-rays via the process of ICS^{6,26}. A typical x-ray beam profile, obtained from the CsI detector, is shown in Fig. 1(b). A complete set of data from all detectors, obtained in a single shot, is shown in Fig. 1(c–f). The dispersed image of the electron beam on the LANEX screen, shown in Fig. 1(c), is used to obtain the spectrum of the electron beam, shown in Fig. 1(d). The image of the x-ray beam on the CdTe detector (with charge sharing correction) for a single shot is shown in Fig. 1(e). The pulse height information is converted to energy using the measured response function of the detector. The resulting x-ray spectrum is shown in Fig. 1(f) (red curve). The black curve in Fig. 1(f) shows the simulated x-ray spectrum. Spectroscopic imaging allowed us to precisely measure the x-ray energy spread, which was found to be $24 \pm 2\%$. This energy spread is comparable to the x-ray bandwidth from conventional RF-LINAC-based Compton sources³⁴, and, to the best of our knowledge, is the narrowest yet reported from an all-laser ICS x-ray light source. Prior results reported energy spreads of 40%³ and 50%⁶.

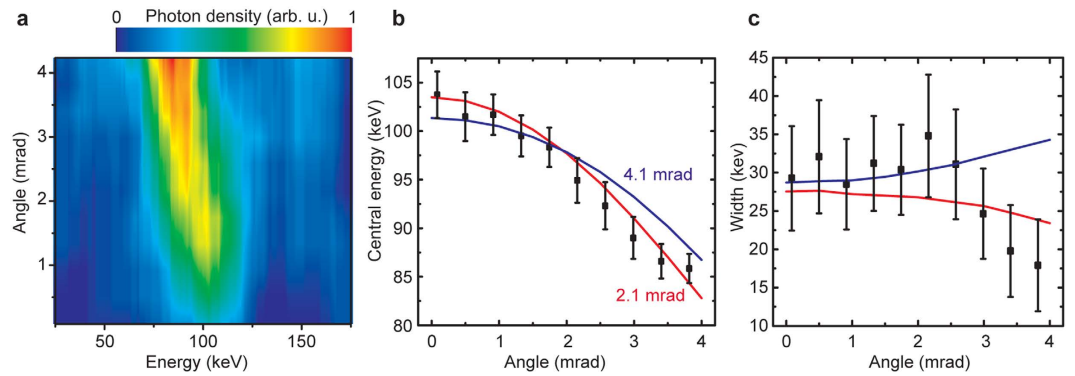


Figure 2. Single-shot angular-resolved x-ray spectrum measured using spectroscopic x-ray imaging. (a) X-ray photon spectrum as a function of polar angle. (b) Mean energy of the x-rays as a function of polar angle. (c) Dependence of the spectral width (FWHM) on the polar angle. Electron beam parameters were: central energy 65 ± 1 MeV; energy spread (FWHM) 8.9 ± 0.1 MeV; and divergence (FWHM) 4.1 ± 0.4 mrad (measured on the LANEX screen). Blue curves on (b,c) show simulated dependences based on these electron beam parameters. Red curves on (b,c) show simulated dependences based on electron beam parameters, obtained from angular-resolved x-ray spectrum: central energy 66 ± 1 MeV; energy spread (FWHM) 8.5 ± 3.5 MeV; and divergence (FWHM) 2.1 ± 0.7 mrad. Error bars represent 95% confidence bands, calculated based on least-squares fits of spectral data. Photon flux at the source is $\sim 10^4$. See details on this measurement in the supplementary.

The spectroscopic x-ray imaging detector allowed us to measure angular-dependent ICS x-ray spectrum for every shot; the result is shown in Fig. 2(a). We fitted the spectra, corresponding to individual polar angles, with Gaussian functions, and extracted the resulting dependencies of central energy and energy spread on angle. The dependence of central energy of the x-rays on polar angle, shown in Fig. 2(b), arises from the dependence of the resonant scattered frequency on the polar angle (see Methods, eq. 2). The dependence of the spectral width on the polar angle, shown in Fig. 2(c), is more complex and requires accounting for both the spectral and angular characteristics of the electron beam.

The angular-resolved spectral measurements were used to determine the parameters of the electron beam. To this end, ICS simulations were performed (see Methods for details), in which three parameters of the electron beam were varied: central energy, energy spread, and divergence. The electron beam parameters could then be obtained, such that the computed and measured angular-resolved x-ray spectra coincide. For the x-ray spectrum shown in Fig. 2, we obtained the following parameters of the corresponding electron beam: central energy (66 ± 1 MeV); energy spread (8.5 ± 3.5 MeV); and divergence (2.1 ± 0.7 mrad). The angular dependence of the x-ray central energy and spread on polar angle for these electron beam parameters inferred from our model are shown in Fig. 2(b,c) as red curves. The computed parameters described the electron beam at the exit of the accelerator structure. For the same electron beam, we also measured these parameters again after 40 cm of propagation using the magnetic spectrometer and LANEX imaging screen. The measured values for the central energy and energy spread are 65 ± 1 MeV and 8.9 ± 0.1 MeV, respectively.

These experimental results show that space-charge effects do not affect the spectrum of the electron beam (on account of its high beam energy), which is found to be consistent with numerical simulations. At the same time, the electron beam divergence after 40 cm of propagation (4.1 ± 0.4 mrad) is twice what it is at the source. This increase arises from space-charge effects, as will be explained in detail later.

Figure 2(b,c) shows that performing only an on-axis measurement of ICS x-rays is not sufficient to obtain electron beam divergence at the accelerator exit. The difference between ICS x-rays generated with 2.1 and 4.1 mrad electron beams (red and blue curves, respectively) becomes pronounced only when the off-axis part of the x-ray spectrum is taken into consideration. See the supplementary section for a discussion on how on- and off-axis ICS spectral measurements affect electron beam measurement precision.

Knife-edge measurements were performed to determine the source size of both the x-ray and electron beams (it should be the same for both, since the scattering laser pulse is much larger than the electron beam at the interaction point). A 2-mm thick steel pattern with different slits was placed at a distance of 2 m from the source; its shadows were imaged at a distance of 5.3 m with an image plate (30- μ m pixel size), yielding a magnification of 2.7. To obtain sufficiently high signal on the image plate, 100 shots were accumulated. An area with an edge shadow on the captured image (shown as a white box on Fig. 3(a)) was chosen, and its profile was plotted (see Fig. 3(b)). Each point on the profile plot shows the median of a row on the image plate picture. The use of the median improves the signal-to-noise ratio of the signal by filtering out outliers. The edge shadow profile is a convolution of the intensity distribution of the x-ray source at its origin and the edge transmission. Assuming a Gaussian intensity distribution of the source and step-transmission function of the edge, one should expect a Gauss error function as a shadow profile, with a width depending on the x-ray's source size. After pointing fluctuation correction (2 mrad RMS), we obtained $\sigma_r = 4 \pm 1$ μ m (RMS) as a final value for the source size. Such a small source size is ideal for radiography, since it permits resolution of microscopic features¹⁵. This also represents an improvement on the best results obtained by means of a different approach: namely, scanning the scattering laser pulse

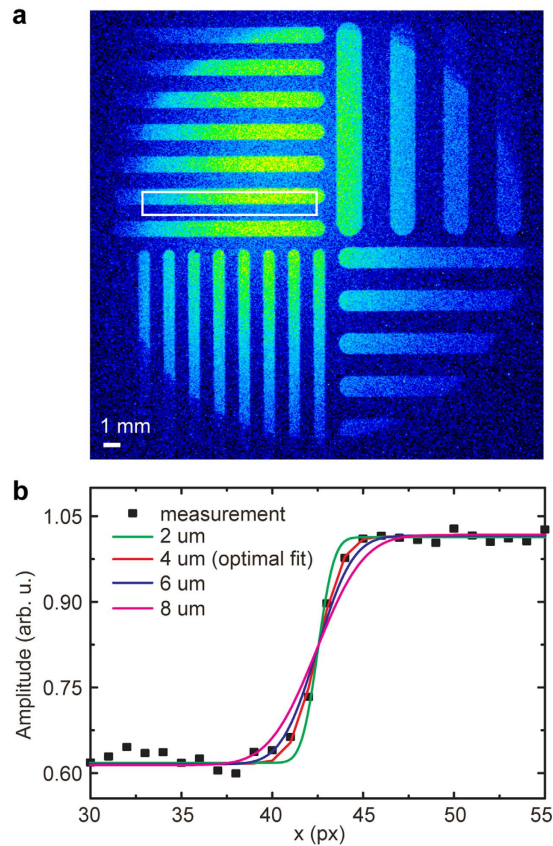


Figure 3. The x-ray and electron beams' source size measurement. (a) Image of the test pattern (taken with an image plate). White box shows the area used for the source size analysis. (b) Intensity profile across the edge of the pattern (black squares) and it fits with Gauss error functions (solid lines). Red curve corresponds to an optimal fit.

across the electron beam (5 ± 3 μm RMS)²⁶. Even though the presented measurement is multiple-shot (and might therefore overestimate source-size), it can be performed in a single shot given a high enough x-ray photon flux.

The emittance of the electron beam is determined by combining the source size measurement with the parameters obtained from x-ray spectroscopic imaging. The normalized electron beam transverse emittance ε_{nt} is computed using the formula $\varepsilon_{nt} = \beta\gamma\sigma_{\theta}\sigma_r$, where β is the ratio of electron speed to the speed of light, γ is the electron beam Lorentz factor, σ_{θ} is the electron beam RMS divergence, and σ_r is the electron beam RMS source-size. We obtained the $\varepsilon_{nt} = 0.15 \pm 0.06$ $\pi\text{mm mrad}$ value measured at 1.5 mm from the exit of the accelerator. This value is on par with the lowest transverse emittance measured so far for an LWFA electron beam. The uncertainty can be improved by using a detector with a larger number of pixels. We also verified that the emittance value computed using this definition is consistent with the standard definition of emittance: $\varepsilon_x = \gamma\beta\sqrt{\langle x^2 \rangle \langle x'^2 \rangle - \langle xx' \rangle^2}$. This was accomplished by reconstructing the phase space of the electron beam using measured parameters, and then computing the emittance based on the statistical definition.

Theoretical models^{22,33} have previously predicted emittance growth for laser-driven electron beams after they exit the accelerator and propagate in free space. Our results qualitatively agree with these predictions. In order to quantitatively determine the extent of emittance growth in our case, we performed numerical calculations that take into account the measured characteristics of the electron beam and the specific experimental geometry. The electron beam phase space was constructed using the measured energy spectrum and source size. The temporal duration was assumed to be 10 fs at the source consistent with prior measurements.

The evolution of the beam is calculated using a particle-tracking code based on an adaptive mesh and including the effects of space charge³⁵. The measured electron beam parameters (energy, energy spread, spot-size, and divergence) fix the initial emittance of the beam. We assumed the origin to be the point where the plasma effects become negligible. Figure 4 shows the evolution of beam divergence and emittance as a function of propagation distance. The former increases rapidly over the first few mm of propagation and then reaches a limiting value. This arises from the fact that as the transverse spatial extent of the beam increases, the space-charge driven force reduces in magnitude and eventually becomes negligible. The transverse emittance, determined by both the size and angular spread of the beam, increases monotonically, and is more than doubled at 1 m compared to that at the source. In our experiments, we performed measurements of the electron beam parameters at locations A and B, the former by means of ICS, and the latter using a fluorescent screen. It is clear that the divergence growth becomes negligible beyond 3 cm. The expansion rate significantly increases for beams with higher charge or lower

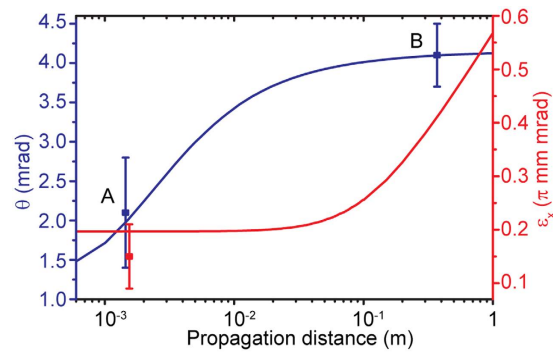


Figure 4. Evolution of the electron beam (divergence and normalized transverse emittance) after exit from the plasma. The divergence, calculated from the rate of change of the transverse beam size, increases rapidly over the first few mm and then reaches a limiting value while the emittance monotonically increases. Labels A and B identify locations that correspond to experimental measurements. The beam at location A is probed by the ICS technique, while the measurement at location B relies on the angular size measured on a fluorescent screen (assuming mostly straight electron trajectories). The electron beam is assumed to have an energy of 65 MeV, energy spread of 10%, and charge of 10 pC.

energy. We investigated the effects of the pulse duration on the computed results and found them to be not significant within a factor of two change in the assumed temporal duration of the electron pulse (10 fs).

Based on the measurements described previously, the beam divergence is 2.1 ± 0.7 mrad at 1.5 mm from the source (measured using single-shot spectroscopic x-ray imaging) and 4.1 ± 0.4 mrad on a fluorescent screen located at 0.37 m from the source. By comparing these values to that shown in Fig. 4, it is clear that there is excellent agreement between the measured and calculated divergence. The normalized transverse emittance determined using $\varepsilon_{nt} = \beta\gamma\sigma_\theta\sigma_r$ is dependent on location, and is significantly overestimated for measurements performed at a large distance from the source. Such limitations would be applicable to measurements performed using the pepper-pot method. It should be noted that our measurement might have slightly overestimated the value of emittance, since the electron beam was still allowed to propagate a fraction of a mm after exiting the down-ramp, before it was overlapped with the scattering laser beam. However, the simulations show that this effect is negligible (notice no change in emittance over the first few cm of propagation, red curve in Fig. 4). Also, the measured beam divergence might differ from the one inside the plasma, because of beam focusing on the plasma down-ramp²⁹.

The measured value of the LWFA electron beam emittance we report here is lower than most of those previously reported in part because the measurement is performed at the source before the emittance degrades. Previous measurements were made with the pepper-pot technique^{20,23–25} and the quadrupole-scan method²⁹ (even though the latter measurement was performed in a regime where space-charge effects were negligible, which is not true in our case). The transverse emittance we report also matches prior estimates for the electron-bunch emittance in the plasma, which were based on a combination of betatron-emission measurements and analytical models^{27,28,36}. The precision of the technique we demonstrate can be further improved by extracting more information out of the angular-resolved x-ray spectrum, as well as utilizing the x-ray spatial profile.

In summary, we used the novel technique of spectroscopic imaging of ICS x-rays to non-destructively measure the intrinsic normalized transverse emittance of the LWFA electron beam immediately at the exit of the accelerator structure. The measured emittance is comparable to the best conventional LINAC accelerators. Ultra-small transverse emittance (ε_{nt}) and source-size (σ_r) of the beam translate into ultra-high spatial coherence ($L_c \propto \sigma_r / \varepsilon_{nt}$)³⁷, which is critical for applications such as ultra-fast electron diffraction. Our results have direct implications for narrowband ICS x-ray sources where high-charge beams with low-emittance are needed to maximize x-ray brightness and limit energy spread³⁸. The ultra-small transverse emittance of the electron beam allowed us to demonstrate record-low energy spread of the all-laser ICS x-rays (24%), which is comparable to the x-ray bandwidth from conventional RF-LINAC-based Compton sources. Our technique can also be used to study the emittance growth of LWFA electron beams as they propagate through plasma-vacuum interface, providing critical insights necessary to minimize emittance growth on the interface³⁹, or to optimize the coupling between stages in multiple-staged LWFA or a conventional beam transport line^{40,41}. Since the technique is single-shot and does not require scanning^{26,29}, it is suitable for electron beams that have shot-to-shot instability. The technique of spectroscopic x-ray imaging also holds promise to provide robust signatures of nonlinear Thomson scattering⁴² and radiation reaction⁴³ in future ultra-high-intensity laser experiments.

Methods

Laser system. High-energy pulses from the Ti:Sapphire laser system were split at the end of the amplification chain using a 80% reflecting (20% transmitting) beam splitter and were independently compressed using 2-grating pulse compressors. The 80% reflected beam was compressed to 34 fs and focused by a $f/14$ parabolic mirror to a 20 μm (FWHM) Gaussian focal spot. An adaptive optic loop composed of a deformable mirror and a wavefront sensor was used to compensate the optical aberrations⁴⁴. We also used an adaptive closed loop to compensate spectral phase distortion⁴⁵. This beam with energy of 1.4 J was used to drive a laser wakefield by focusing onto a double-nozzle gas target⁴ at 2 mm height above the nozzle orifice. The 20% transmitted beam with 0.3 J energy

was compressed to 40 fs and focused to a 20- μm (FWHM) Gaussian focal spot by another $f/14$ parabolic mirror to normalized field strength $a_0 = 0.7$. It was used to generate x-rays by scattering off the LWFA electron beam with the focus of the scattering pulse being located 1.5 mm after the end of the second gas nozzle.

Laser wakefield electron acceleration. The first and second nozzles (both 0.5×2 mm slits) of the double-jet gas target⁴ were operated with 99/1 mixture of helium and nitrogen and pure helium, respectively. The nozzles were separated by 0.5-mm gap. Three-dimensional density profiles of the gas flow from the nozzle were measured offline with a Mach-Zander interferometer and reconstructed using the SIRT tomography algorithm⁴⁶. Energy of the electron beams was controlled by the second gas jet density. We used a magnetic spectrometer to characterize the energy spectra of the laser-produced electron beams. The spectrometer consisted of a round magnet (0.8 T, 19 cm diameter) and charge-calibrated LANEX screen imaged by a 12-bit CCD. The LANEX was located outside of the x-ray beam path to allow simultaneous measurement of both x-ray and electron beams. For the energy range reported in this work, the spectrometer had a resolution of 2%.

Spectroscopic x-ray imaging. The energy spectrum of the ICS x-rays was measured using the HEXITEC spectroscopic imaging detector⁴⁷. This system contains an energy-resolving Application-Specific Integrated Circuit (ASIC) which is bump-bonded directly to a 1-mm thick cadmium telluride (CdTe) detector. The output signal from each pixel is directly proportional to the energy deposited by an x-ray absorbed in the CdTe crystal. The detector consists of an array of 80×80 pixels on a $250 \mu\text{m}$ pitch with a total area of $20.35 \text{ mm} \times 20.45 \text{ mm}$. The position and precise energy deposited by each absorbed x-ray is recorded for each 100 μs frame. The recorded data is corrected for charge sharing events where x-rays that share energy between two or more pixels are removed. Without correction these shared events would incorrectly appear as multiple lower energy photons⁴⁸. Each pixel is able to resolve x-ray energies with a resolution of 0.8 keV at 59.5 keV and 1.5 keV at 141 keV⁴⁷. We carefully shielded the detector from background radiation comprised primarily of secondary radiation produced by electrons scattered off the chamber walls and the electron beam dump. The shielding was based on MCNP simulations of the background radiation in the experimental area. As a result, we were able to take measurements with negligible background. The distance between the detector and the source was chosen to be ~ 3 m in order to ensure that the photon flux on the detector was < 0.1 photon/pixel. Based on Poisson statistics, we computed that the probability of 2 photons hitting a pixel is $< 1\%$ and therefore pile-up effects could be neglected. The detector was aligned with the drive laser beam. X-ray beam position on the detector was determined by analyzing the spatially-resolved x-ray spectra.

ICS modeling. In order to model the scattering process, we used the well-known result for the cross-section for Thomson scattering for a single electron (averaged over the azimuthal angle), given by

$$\frac{d^2N}{d\omega d\Omega}(\omega, \gamma, \theta) = \frac{\alpha\gamma^2 N_0 a_0^2}{\omega_R} \left[\frac{1 + \gamma^4 \theta^4}{(1 + \gamma^2 \theta^2)^4} \right] R(\omega, \omega_R), \quad (1)$$

where ω —frequency of the laser light, Ω —solid angle, α —fine structure constant, γ is the electron Lorentz factor, N_0 —number of laser oscillations the electron sees, and $a_0 = 0.85 \times 10^{-9} \lambda[\mu\text{m}](I[\text{W}/\text{cm}^2])^{1/2}$ —dimensionless laser strength parameter (λ —laser wavelength, I —intensity), θ —polar observation angle⁴⁹. The resonance frequency ω_R of the scattered light is given as

$$\omega_R = \frac{2\gamma^2(1 - \cos \varphi)}{1 + a_0^2/2 + \gamma^2\theta^2}\omega, \quad (2)$$

where φ is the collision angle between the electron and the laser pulse (170° in our geometry) and ω is the laser pulse frequency. The resonance function $R(\omega, \omega_R)$ depends on the laser pulse shape. For long laser pulses ($N_0 \gg 1$, $N_0 \sim 10$ for our experiment), $R(\omega, \omega_R) \propto \delta R(\omega - \omega_R)$ so that photons with specific energies are emitted along specific angles (not cones). In order to compute the scattered photon spectrum as a function of angle for the electron beams used in our experiment, equation (1) is integrated as follows:

$$\frac{d^2N_{\text{beam}}}{d\omega d\Omega}(\omega, \theta) = \int d\gamma \int d\theta_e \frac{d^2N_{\text{single}}}{d\omega d\Omega}(\omega, \gamma, \theta - \theta_e) \times f_e(\gamma, \theta_e), \quad (3)$$

The quantity $f_e(\gamma, \theta_e)$ is the energy-angle distribution of the LWFA electron beam. The Supplementary Material provides an analysis of the range of validity of the model, and a cross-check with a fully relativistic 3D numerical model of ICS.

References

1. Hooker, S. Developments in laser-driven plasma accelerators. *Nature Photonics* **7**, 775–782 (2013).
2. Umstadter, D. P. All-laser-driven Thomson X-ray sources. *Contemporary Physics* **56**, 417–431 (2015).
3. Banerjee, S. *et al.* Stable, tunable, quasimonoenergetic electron beams produced in a laser wakefield near the threshold for self-injection. *Physical Review Special Topics-Accelerators and Beams* **16**, 031302 (2013).
4. Golovin, G. *et al.* Tunable monoenergetic electron beams from independently controllable laser-wakefield acceleration and injection. *Physical Review Special Topics-Accelerators and Beams* **18**, 011301 (2015).
5. Khrennikov, K. *et al.* Tunable All-Optical Quasimonoenergetic Thomson X-Ray Source in the Nonlinear Regime. *Phys. Rev. Lett.* **114**, 195003 (2015).
6. Powers, N. D. *et al.* Quasi-monoenergetic and tunable X-rays from a laser-driven Compton light source. *Nature Photonics* **8**, 29–32 (2014).

7. Liu, C. *et al.* Generation of 9 MeV γ -rays by all-laser-driven Compton scattering with second-harmonic laser light. *Opt. Lett.* **39**, 4132–4135 (2014).
8. Lundh, O. *et al.* Few femtosecond, few kiloampere electron bunch produced by a laser-plasma accelerator. *Nature Physics* **7**, 219–222 (2011).
9. Debus, A. *et al.* Electron bunch length measurements from laser-accelerated electrons using single-shot THz time-domain interferometry. *Phys. Rev. Lett.* **104**, 084802 (2010).
10. Albert, F. *et al.* Laser wakefield accelerator based light sources: potential applications and requirements. *Plasma Phys. Controlled Fusion* **56**, 084015 (2014).
11. Chin, A. *et al.* Ultrafast structural dynamics in InSb probed by time-resolved x-ray diffraction. *Phys. Rev. Lett.* **83**, 336–339 (1999).
12. Reckenthäler, P. *et al.* Time-Resolved Electron Diffraction from Selectively Aligned Molecules. *Phys. Rev. Lett.* **102**, 213001 (2009).
13. Corde, S. *et al.* Femtosecond x rays from laser-plasma accelerators. *Reviews of Modern Physics* **85**, 1 (2013).
14. Jones, R. L. *et al.* Small angle x-ray scattering for sub-100 nm pattern characterization. *Appl. Phys. Lett.* **83**, 4059–4061 (2003).
15. Courtois, C. *et al.* High-resolution multi-MeV x-ray radiography using relativistic laser-solid interaction. *Physics of Plasmas (1994-present)* **18**, 023101 (2011).
16. Kneip, S. *et al.* X-ray phase contrast imaging of biological specimens with femtosecond pulses of betatron radiation from a compact laser plasma wakefield accelerator. *Appl. Phys. Lett.* **99**, 093701 (2011).
17. Fourmaux, S. *et al.* Single shot phase contrast imaging using laser-produced Betatron x-ray beams. *Opt. Lett.* **36**, 2426–2428 (2011).
18. Malka, V. *et al.* Principles and applications of compact laser-plasma accelerators. *Nat Phys* **4**, 447–453 (2008).
19. Cianchi, A. *et al.* Challenges in plasma and laser wakefield accelerated beams diagnostic. *Nuclear Instruments and Methods in Physics Research Section A: Accelerators, Spectrometers, Detectors and Associated Equipment* **720**, 153–156 (2013).
20. Brunetti, E. *et al.* Low emittance, high brilliance relativistic electron beams from a laser-plasma accelerator. *Phys. Rev. Lett.* **105**, 215007 (2010).
21. Migliorati, M. *et al.* Intrinsic normalized emittance growth in laser-driven electron accelerators. *Physical Review Special Topics-Accelerators and Beams* **16**, 011302 (2013).
22. Chao, A. W., Pitthan, R., Tajima, T. & Yermian, D. Space charge dynamics of bright electron beams. *Physical Review Special Topics-Accelerators and Beams* **6**, 024201 (2003).
23. Fritzier, S. *et al.* Emittance measurements of a laser-wakefield-accelerated electron beam. *Phys. Rev. Lett.* **92**, 165006 (2004).
24. Sears, C. M. *et al.* Emittance and divergence of laser wakefield accelerated electrons. *Physical Review Special Topics-Accelerators and Beams* **13**, 092803 (2010).
25. Manahan, G. *et al.* Characterization of laser-driven single and double electron bunches with a permanent magnet quadrupole triplet and pepper-pot mask. *New Journal of Physics* **16**, 103006 (2014).
26. Chen, S. *et al.* MeV-Energy X Rays from Inverse Compton Scattering with Laser-Wakefield Accelerated Electrons. *Phys. Rev. Lett.* **110**, 155003 (2013).
27. Kneip, S. *et al.* Characterization of transverse beam emittance of electrons from a laser-plasma wakefield accelerator in the bubble regime using betatron x-ray radiation. *Physical Review Special Topics-Accelerators and Beams* **15**, 021302 (2012).
28. Plateau, G. *et al.* Low-emittance electron bunches from a laser-plasma accelerator measured using single-shot x-ray spectroscopy. *Phys. Rev. Lett.* **109**, 064802 (2012).
29. Weingartner, R. *et al.* Ultralow emittance electron beams from a laser-wakefield accelerator. *Physical Review Special Topics-Accelerators and Beams* **15**, 111302 (2012).
30. Leemans, W. *et al.* X-ray based subpicosecond electron bunch characterization using 90 degrees Thomson scattering. *Phys. Rev. Lett.* **77**, 4182–4185 (1996).
31. Chouffani, K., Harmon, F., Wells, D., Jones, J. & Lancaster, G. Determination of electron beam parameters by means of laser-Compton scattering. *Physical Review Special Topics-Accelerators and Beams* **9**, 050701 (2006).
32. Jochmann, A. *et al.* High Resolution Energy-Angle Correlation Measurement of Hard X Rays from Laser-Thomson Backscattering. *Phys. Rev. Lett.* **111**, 114803 (2013).
33. Fubiani, G., Qiang, J., Esarey, E., Leemans, W. & Dugan, G. Space charge modeling of dense electron beams with large energy spreads. *Physical Review Special Topics-Accelerators and Beams* **9**, 064402 (2006).
34. Albert, F. *et al.* Isotope-specific detection of low-density materials with laser-based monoenergetic gamma-rays. *Opt. Lett.* **35**, 354–356 (2010).
35. Pöplau, G., Van Rienen, U., Van der Geer, B. & De Loos, M. Multigrid algorithms for the fast calculation of space-charge effects in accelerator design. *Magnetics, IEEE Transactions on* **40**, 714–717 (2004).
36. Albert, F. *et al.* Angular dependence of betatron x-ray spectra from a laser-wakefield accelerator. *Phys. Rev. Lett.* **111**, 235004 (2013).
37. Van Oudheusden, T. *et al.* Electron source concept for single-shot sub-100 fs electron diffraction in the 100 keV range. *J. Appl. Phys.* **102**, 093501 (2007).
38. Hartemann, F. V. *et al.* Compton scattering X-ray sources driven by laser wakefield acceleration. *Phys. Rev. ST Accel. Beams* **10**, 011301 (2007).
39. Dornmair, I., Floettmann, K. & Maier, A. Emittance conservation by tailored focusing profiles in a plasma accelerator. *Physical Review Special Topics-Accelerators and Beams* **18**, 041302 (2015).
40. Thaury, C. *et al.* Demonstration of relativistic electron beam focusing by a laser-plasma lens. *Nature communications* **6**, doi: 10.1038/ncomms7860 (2015).
41. van Tilborg, J. *et al.* Active Plasma Lensing for Relativistic Laser-Plasma-Accelerated Electron Beams. *Phys. Rev. Lett.* **115**, 184802 (2015).
42. Chen, S. Y., Maksimchuk, A. & Umstadter, D. Experimental observation of relativistic nonlinear Thomson scattering. *Nature* **396**, 653–655 (1998).
43. Di Piazza, A., Hatsagortsyan, K. Z. & Keitel, C. H. Strong Signatures of Radiation Reaction below the Radiation-Dominated Regime. *Phys. Rev. Lett.* **102**, 254802 (2009).
44. Zhao, B. *et al.* Wavefront-correction for nearly diffraction-limited focusing of dual-color laser beams to high intensities. *Optics express* **22**, 26947–26955 (2014).
45. Liu, C. *et al.* *Adaptive spectral-phase control for laser wakefield electron acceleration* (CLEO: Applications and Technology, Optical Society of America, 2014).
46. Golovin, G. *et al.* Tomographic imaging of nonsymmetric multicomponent tailored supersonic flows from structured gas nozzles. *Appl. Opt.* **54**, 3491–3497 (2015).
47. Seller, P. *et al.* Pixelated Cd (Zn) Te high-energy X-ray instrument. *Journal of Instrumentation* **6**, C12009 (2011).
48. Veale, M. *et al.* Measurements of charge sharing in small pixel CdTe detectors. *Nuclear Instruments and Methods in Physics Research Section A: Accelerators, Spectrometers, Detectors and Associated Equipment* **767**, 218–226 (2014).
49. Rykovanov, S. *et al.* Quasi-monoenergetic femtosecond photon sources from Thomson Scattering using laser plasma accelerators and plasma channels. *Journal of Physics B: Atomic, Molecular and Optical Physics* **47**, 234013 (2014).

Acknowledgements

We thank K. Brown and J. Mills for operating the laser system, C. Petersen for performing data acquisition, H. Karwowski for providing the test pattern used for source size measurements, and N. Glasco for proofreading the manuscript. This material is based on work supported by the National Science Foundation under Grant No. PHY-153700 (ultra-low emittance electron beams); US Department of Energy (DOE), Office of Science, Basic Energy Sciences (BES), under Award # DE-FG02-05ER15663 (ultrafast x-ray science); the Air Force Office for Scientific Research, FA9550-11-1-0157 (high-field laser-electron scattering); and the Department of Homeland Security Domestic Nuclear Detection Office, under competitively awarded contract HSHQDC-13-C-B0036 (low-dose x-ray radiography). This support does not constitute an express or implied endorsement on the part of the Government.

Author Contributions

G.G., S.B. and D.U. conceived the experiment. G.G., S.B., C.L., S.C., J.Z., B.Z., P.Z., M.V. and M.W. performed the experiments. G.G., M.V. and M.W. analyzed the data. G.G. performed the ICS simulations and S.B. computed the space charge driven evolution of the electron beam. M.V., M.W. and P.S. provided the HEXITEC spectroscopic imaging detector. G.G., S.B. and D.U. co-wrote the manuscript with contributions from all authors.

Additional Information

Supplementary information accompanies this paper at <http://www.nature.com/srep>

Competing financial interests: The authors declare no competing financial interests.

How to cite this article: Golovin, G. *et al.* Intrinsic beam emittance of laser-accelerated electrons measured by x-ray spectroscopic imaging. *Sci. Rep.* **6**, 24622; doi: 10.1038/srep24622 (2016).



This work is licensed under a Creative Commons Attribution 4.0 International License. The images or other third party material in this article are included in the article's Creative Commons license, unless indicated otherwise in the credit line; if the material is not included under the Creative Commons license, users will need to obtain permission from the license holder to reproduce the material. To view a copy of this license, visit <http://creativecommons.org/licenses/by/4.0/>